

We are not the 99 percent: quantifying asphericity in the distribution of Local Group satellites

Jaime E. Forero-Romero¹ , Verónica Arias¹

¹ *Departamento de Física, Universidad de los Andes, Cra. 1 No. 18A-10 Edificio Ip, CP 111711, Bogotá, Colombia*

1 March 2018

ABSTRACT

We use numerical simulations to build an explicit probability distribution for the asphericity in the satellite distribution around galaxies similar to the Local Group (LG) in the Lambda Cold Dark Matter (LCDM) paradigm. This allows us to estimate the atypicality of the satellite distributions in the LG even when the underlying simulations do not have enough systems that fully resemble the LG. We demonstrate the method using three different simulations: Illustris-1, Illustris-1-Dark and ELVIS. Detailed results differ among the simulations suggesting a strong influence of the typical Dark Matter (DM) halo mass in the LG samples and simulated baryonic effects. However, there are three common trends. First, at most of 2% the pairs are expected to have satellite distributions with the same asphericity as the LG; second, between 27% to 56% of the pairs have a halo with a satellite distribution as aspherical as in M31; and third, at most 3% of the pairs have a satellite distribution as planar as in the MW. The brightest satellites in the M31 galaxy have a rather typical distribution in the LCDM context, while the MW distribution is atypical in this respect. These quantitative results place the LG at the level of a 3σ outlier in the LCDM paradigm. We suggest that understanding the reasons for this atypicality will require quantifying the asphericity probability distribution as a function of halo mass and large scale environment. The approach presented here can facilitate that kind of study and other comparisons between different numerical setups and choices to study satellites around LG pairs in simulations.

Key words: Galaxies: halos — Galaxies: statistics — Dark Matter — Methods: numerical

1 INTRODUCTION

The spatial distribution of satellite galaxies around our Milky Way (MW) and the M31 galaxy is becoming a stringent test for structure formation theories in an explicit cosmological context. This started with the suggested existence of a Magellanic Plane, a flattened structure of satellite galaxies and globular clusters around the MW, by Kunkel & Demers (1976) and Lynden-Bell (1976). Forty years later Kroupa et al. (2005) quantified that the highly planar distribution of the 11 classical MW satellites has less than a 0.5% chance to happen by chance if the parent distribution is spherically symmetric, interpreting this as a challenge to the Lambda Cold Dark Matter (LCDM) paradigm. The same year it was recognized, using numerical simulations, that this comparison was unfair given that Dark Matter halos in LCDM are expected to be triaxial and not spherical. Nevertheless, some

estimates of the chances to find simulated satellites as planar as in the MW were as low as 2% (Zentner et al. 2005) while others expected planar satellite configurations in every DM halo (Libeskind et al. 2005).

Later, Metz et al. (2007) used simulations to confirm the low chances ($< 0.5\%$) found in Kroupa et al. (2005). This result was challenged by Libeskind et al. (2009) who continued to report high chances to find a planar configuration; two more recent numerical experiments with high resolution simulations (Starkenburg et al. (2013) and Sawala et al. (2016)) reported contradicting results (low and high chances to find the observational result, respectively) but precise figures were not quoted in these three reports. Meanwhile, Wang et al. (2013) and Pawłowski & McGaugh (2014) published the results of new tests using high resolution simulations and cosmological volumes arriving at a chance of 6% and 0.77%, respectively, to have a satellite distribution as triaxial as the observations.

In the case of M31, observational studies have found a

* je.forero@uniandes.edu.co

planar satellite distribution in a special subset of 15 satellites out of the total population of 27 satellites (Conn et al. 2013; Ibata et al. 2013), although considering the satellites ranked by luminosity does not show any special feature. All published studies agree on the point that the spatial distribution of the 15 to 27 brightest satellites are consistent with spherically symmetric distribution and easy to reproduce in LCDM simulations (Koch & Grebel 2006; Metz et al. 2007; Conn et al. 2013). Table 1 and Table 2 summarize some more details on the results we have just mentioned ¹.

Some of the difficulty in trying to reconcile and understand the seemingly conflicting or inconclusive results on the MW has its origin on the frequentist fashion generally used to compute probabilities. Usually, this process starts by building a high level parent sample in the simulation and then counting how many elements has the subset meeting some criteria. This has two inconvenients. The first is that the probability estimate is made against whatever turns out to be typical in each simulation. A fair comparison across simulations would require first characterizing all the simulations at the high level parent samples, something that is difficult to do in practice. The second inconvenient is that the systems that fully resemble the LG (i.e. its stellar mass content, morphology or kinematics) have a low cosmological number density, this means that for the current cosmological volumes in simulations the high level parent sample has a small size, making it hard to derive robust probabilities by counting. In this paper we present and demonstrate a method to overcome these two limitations.

We control the first effect by setting as a direct point of reference a spherical satellite distribution and not the simulations themselves. The spherical satellite distribution is built from the data itself (observational or simulated) by randomizing the angular position of each satellite around the central galaxy and keeping its radial distance fixed (Pawlowski et al. 2017). We characterize the satellites in terms of the scalars describing its deviation from the spherical distribution. We then build an explicit analytic probability distribution for the asphericity; this solves the problem of having a common reference point to compare simulations. We use a simulation to estimate the parameters in this distribution to later use it as a parent sample to generate any desired number of samples that are by construction statistically compatible with the simulation; thus overcoming the problem of having a small number of systems in the parent simulations.

To summarize, we use asphericity to characterize on equal footing simulations and observations. Then, we build an explicit probability distribution for the asphericity and use simulations to estimate its free parameters. Finally, we use these distributions to generate large numbers of samples and directly estimate the number of systems meeting a desired set of criteria.

The rest of the paper describes in detail our implementation and results. It is structured as follows. In Section 2 we list the sources of the observational and simulated data to be used throughout the paper. In Section 3 we describe the methods we use to build halo pairs and characterize their

satellite distributions. In Section 4 we present our results to finally conclude in Section 5.

2 DATA SAMPLES

2.1 Observational Data

The base for our analysis is the catalog compiled by Pawlowski et al. (2014) which reports information on all galaxies within 3 Mpc around the Sun to that date. Detailed description of the compiled catalog can be found in Pawlowski et al. (2013), here we summarize the relevant features for the current study. The information in the catalogue is based on the catalogue compiled by McConnachie (2012). The distance estimates are based on resolved stellar populations. We use three dimensional positions in a cartesian coordinate system as computed by Pawlowski et al. (2013). In this coordinate system the z -axis points towards the Galactic north pole, the x -axis points in the direction from the Sun to the Galactic center, and the y -axis points in the direction of the Galactic rotation.

For both the M31 and MW we only use the 11 to 15 brightest satellites (using M_V magnitudes) within a distance of 300kpc from its central galaxy. The satellites included for the MW analysis are: LMC, SMC, Canis Major, Sagittarius dSph, Fornax, Leo I, Sculptor, Leo II, Sextans I, Carina, Ursa Minor, Draco, Canes Venatici (I), Hercules and Bootes II. The satellites included for the M31 analysis are: Triangulum, NGC205, M32, IC10, NGC185, NGC147, Andromeda VII, Andromeda II, Andromeda XXXII, Andromeda XXXI, Andromeda I, Andromeda VI, Andromeda XXIII, LGS 3, and Andromeda III.

2.2 Data from the Illustris project

We use publicly available data from the Illustris Project (Vogelsberger et al. 2014). This suite of cosmological simulations, performed using the quasi-Lagrangian code AREPO (Springel 2010), followed the coupled evolution of dark matter and gas and includes parametrizations to account for the effects of gas cooling, photoionization, star formation, stellar feedback, black hole and super massive black hole feedback. The simulation volume is a cubic box with a $75 \text{ Mpc } h^{-1}$ side. The cosmological parameters correspond to a Λ CDM cosmology consistent with WMAP-9 measurements (Hinshaw et al. 2013).

We extract halo and galaxy information from the Illustris-1 and Illustris-1-Dark simulations, the former simulation includes hydrodynamics and star formation prescriptions while the latter only includes dark matter physics. These simulations have the highest resolution in the current release of the Illustris Project. Illustris-1 has 1820^3 dark matter particles and 1820^3 initial gas volume elements, while Illustris-1-Dark has 1820^3 dark matter particles. This corresponds to a dark matter particle mass of $6.3 \times 10^6 M_\odot$ and a minimum mass for the baryonic volume element of $8.0 \times 10^7 M_\odot$ for Illustris-1 and a dark matter particle mass of $7.6 \times 10^6 M_\odot$ for Illustris-1-Dark. In both simulations the dark matter gravitational softening is 1.4 kpc.

We build a sample of pairs that resemble the conditions in the LG. To construct this sample we select from

¹ Those tables also include the results from this paper using the methodology we describe in the upcoming sections.

Reference	Target Measurement	Parent Simulation	Probability (%)
Koch & Grebel (2006)	RMS width in 15 brightest satellites	Monte Carlo satellite distributions with a power law radial distribution	87 – 99
Metz et al. (2007)	c/a ratio and RMS width in 16 brightest satellites	Monte Carlo from a spherical power law radial distribution	17
Conn et al. (2013)	RMS width in the 27 brightest satellites	Monte Carlo randomized satellite distribution	High
This Work	c/a ratio, b/a ratio and RMS width in 11-15 brightest satellites	24 halos from selected pairs in a cosmological N-body Dark Matter only simulation ($\sim 10^6 M_\odot$ particle mass resolution)	56
This Work	c/a ratio, b/a ratio and RMS width in 11-15 brightest satellites	20 halos from selected pairs in a cosmological N-body hydro simulation ($\sim 10^6 M_\odot$ particle mass resolution)	27
This Work	c/a ratio, b/a ratio and RMS width in 11-15 brightest satellites	12 high resolution DM only N-body simulations ($\sim 10^5 M_\odot$ particle mass resolution) of halo pairs	37

Table 1. Probability to find the triaxiality and/or root mean squared (RMS) height of M31 satellites in LCDM simulations.

Reference	Target Measurement	Parent Simulation	Probability (%)
Kroupa et al. (2005)	RMS width in 11 classical satellites	Monte Carlo from a spherical power law radial distribution.	< 0.5
Libeskind et al. (2005)	c/a ratio of 11 classical satellites	6 high resolution DM only N-body simulations ($\sim 10^5 M_\odot$ particle mass resolution).	High
Zentner et al. (2005)	c/a ratio and disk height in 11 classical satellites	3 high resolution DM only N-body simulations. ($\sim 10^6 M_\odot$ particle mass resolution)	2
Metz et al. (2007)	c/a ratio and RMS width in 11-13 brightest satellites	Monte Carlo from a halo triaxiality distribution from LCDM simulations	< 0.5
Libeskind et al. (2009)	c/a ratio in 11 classical satellites	436 halos from a cosmological N-body simulation ($1.3 \times 10^8 M_\odot$ particle mass)	High
Starkenburg et al. (2013)	c/a ratio in 12 brightest satellites	6 High resolution DM only N-body simulations ($\sim 10^3 M_\odot$ particle mass resolution) of individual halos	Low
Wang et al. (2013)	c/a ratio or RMS width in 11 brightest satellites	1686 halos from a cosmological DM only N-body simulation ($\sim 10^6 M_\odot$ particle mass resolution)	6 or 13
Pawlowski & McGaugh (2014)	c/a and b/a ratio in 11 classical satellites	48 high resolution DM only N-body simulations ($\sim 10^5 M_\odot$ particle mass resolution) of both halo pairs and isolated halos	0.77
Sawala et al. (2016)	c/a ratio in 11 classical satellites	12 high resolution Hydro simulation of halo pairs ($\sim 10^4 M_\odot$ particle mass resolution)	High
This Work	c/a ratio, b/a ratio and RMS width in 11-15 brightest satellites	24 halos from selected pairs in a cosmological N-body Dark Matter only simulation ($\sim 10^6 M_\odot$ particle mass resolution)	3
This Work	c/a ratio, b/a ratio and RMS width in 11-15 brightest satellites	20 halos from selected pairs in a cosmological N-body hydro simulation ($\sim 10^6 M_\odot$ particle mass resolution)	0.6
This Work	c/a ratio, b/a ratio and RMS width in 11-15 brightest satellites	12 high resolution DM only N-body simulations ($\sim 10^5 M_\odot$ particle mass resolution) of halo pairs	0.2

Table 2. Same as Table 1 for the MW satellites.

Illustris-1 all the galaxies with a stellar mass in the range $1 \times 10^{10} M_\odot < M_\star < 1.5 \times 10^{11} M_\odot$. Then we select the pairs with the following conditions.

- For each galaxy A we find its closest galaxy B , if galaxy A is also the closest to halo B , the two are considered as a pair.
- With d_{AB} the distance between the two galaxies and $M_{\star,min}$ the lowest stellar mass in the two galaxies, we dis-

card pairs that have any other galaxy C with stellar mass $M_\star > M_{\star,min}$ closer than $3 \times d_{AB}$ from any of the pair's members.

- The distance d_{AB} is greater than 700 kpc.
- The relative radial velocity between the two galaxies, including the Hubble flow, is $-120 \text{ km s}^{-1} < v_{AB,r} < 0 \text{ km s}^{-1}$.

We find 27 pairs with these conditions. We then select

the pairs where in both halos there are at least 15 detected subhalos, thus discarding pairs with halos with the lowest mass. We end up with a total of 20 pairs in Illustris-1.

In Illustris-1-Dark we use the center of mass position of the 27 pairs in Illustris-1 to find the matching halo pairs. After discarding the pairs with less than 15 detected subhalos in one of the halos we end up with a total of 24 pairs in Illustris-1-Dark. This corresponds to a pair number density of $\sim 2 \times 10^{-5}$ pairs Mpc^{-3} . Appendix A shows the physical properties (stellar masses, maximum circular velocities, radial velocities and separation) of those pairs.

Although Illustris-1 has stellar particles, we do not use their properties to select the satellite population. The smallest galaxies are barely resolved in stellar mass at magnitudes of $M_V = -9$, close to the limit of the 11 “classical” MW satellites, we use instead the dark matter information. Both in Illustris-1 and Illustris-1-Dark we chose the satellite samples by ranking the subhalos in decreasing order of its current maximum circular velocity and select the first N_p halos in the list. Under these conditions the smallest sub-halos are sampled with at least 40 particles. The results presented here correspond to $11 \leq N_p \leq 15$.

2.3 Data from the ELVIS project

We use data from the public release of the Exploring the Local Universe In Simulations (ELVIS) project. For a detailed description of that project and its data we refer the reader to [Garrison-Kimmel et al. \(2014\)](#). Here we summarize the elements relevant to our discussion.

ELVIS data comes from resimulations of dark matter halo pairs selected in dark matter only cosmological simulations. The parent cosmological boxes have a cosmology consistent with the Wilkinson Microwave Anisotropy Probe 7 results.

The ELVIS project used the results from 50 simulation boxes of side length 70.4 Mpc to select pairs with kinematic characteristics similar to the LG. These selection criteria included the following

- The virial mass of each host must be in the range $1 \times 10^{12} M_\odot < M_{\text{vir}} < 3 \times 10^{12} M_\odot$
- The total pair mass must be in the range $2 \times 10^{12} M_\odot < M_{\text{vir}} < 5 \times 10^{12} M_\odot$
- The center of mass separation is in the range $0.6 \leq d \leq 1$ Mpc.
- The relative radial velocity is negative.
- No halos more massive than the least massive halo within 2.8 Mpc and no halos with $M_{\text{vir}} > 7 \times 10^{13}$ within 7 Mpc of the pairs’ center of mass.

This corresponds to a pair number density of $\sim 8 \times 10^{-6}$ pairs Mpc^{-3} , this is a factor ~ 2.5 lower than the pair number density we find in the Illustris-1 data. There were a total of 146 pairs that met those criteria, but only 12 were chosen for resimulation. Additionally, the selected pairs for resimulation have a relative tangential velocity less than 75 km s^{-1} . The dark matter particle resolution in these resimulations is 1.9×10^5 , a thousand times better than Illustris-1. In this paper we only use the results from these 12 resimulated pairs.

Appendix A compares the physical properties (stellar masses, maximum circular velocities, radial velocities

and separation) in those pairs against the results from the Illustris-1 simulations.

3 BUILDING, CHARACTERIZING AND COMPARING SATELLITES SPATIAL DISTRIBUTIONS

3.1 Building Satellite Samples

We compare the joint satellite distributions in the MW and M31 at fixed satellite number, N_p . This means that the magnitude cut corresponding to the faintest satellite included in the sample is different in each case. We make this choice to rule out the influence of satellite numbers in the statistics.

We compute the satellite statistics for 11 up to 15 satellites. The lower limit corresponds to the number of classical MW satellites, while the upper limit corresponds to the minimum number of M31 satellites usually included M31 studies. In simulations we rank the subhalos by their maximum circular velocity, in observations we rank the satellites by its M_V magnitude.

3.2 Describing Samples with the Inertia Tensor

We describe the satellites with the inertia tensor defined by the satellites’ positions.

$$\bar{\mathbf{I}} = \sum_{k=1}^{N_p} [(\mathbf{r}_i - \mathbf{r}_0)^2 \cdot \mathbf{1} - (\mathbf{r}_i - \mathbf{r}_0) \cdot (\mathbf{r}_i - \mathbf{r}_0)^T], \quad (1)$$

where k indexes the set of satellites of interest \mathbf{r}_k are the satellites’ positions, \mathbf{r}_0 is the location of the central galaxy $\mathbf{1}$ is the unit matrix, and \mathbf{r}^T is the transposed vector \mathbf{r} . We use \mathbf{r}_0 as the position of the central galaxy, and not the satellites’ geometrical center, to allow for a fair comparison once the angular positions of the satellites are randomized around this point.

From this tensor we compute its eigenvalues, $\lambda_1 > \lambda_2 > \lambda_3$, and corresponding eigenvectors, $\hat{I}_1, \hat{I}_2, \hat{I}_3$. We define the size of the three ellipsoidal axis as $a = \lambda_1, b = \lambda_2$ and $c = \lambda_3$. We also define $\hat{n} \equiv \hat{I}_1$ as the vector perpendicular to the planar satellite distribution. We also define the Root Mean Squared (RMS) plane width w as the standard deviation of the satellite distances to the plane defined by the vector \hat{n} .

To summarize we characterize the satellite distribution with the following quantities obtained from the inertia tensor:

- RMS plane width, w .
- c/a axis ratio.
- b/a axis ratio.

3.3 Characterizing Asphericity

We compare each satellite distribution against its own spherically randomized distribution. We keep fixed the radial position of every satellite with respect to the central galaxy and then randomize its angular position. We repeat this procedure 1000 times for each satellite distribution and proceed to measure the quantities mentioned in the previous section: $w, c/a$ and b/a . For each quantity we compute the average

	Observations		Randomized Obs.		Normalized Units	
	M31	MW	M31	MW	M31	MW
Plane width (kpc)	59 ± 3	21 ± 2	65 ± 12	45 ± 8	-0.48 ± 0.24	-2.48 ± 0.26
c/a ratio	0.45 ± 0.04	0.25 ± 0.05	0.55 ± 0.10	0.53 ± 0.10	-1.03 ± 0.37	-2.18 ± 0.42
b/a ratio	0.82 ± 0.06	0.80 ± 0.04	0.82 ± 0.07	0.81 ± 0.08	-0.02 ± 0.82	-0.13 ± 0.47

Table 3. Results from observations. Mean values and standard deviations for the different quantities describing the satellite distributions: plane width, c/a ratio and b/a ratio. The first column refers to the results from observational data, the second column uses the spherically randomized version of the observational data, the third column corresponds to the observational data recentered and normalized by the randomized values.

	Illustris-1-Dark		Illustris-1		ELVIS	
	M31	MW	M31	MW	M31	MW
Plane width (kpc)	62 ± 3	61 ± 3	70 ± 4	67 ± 2	70 ± 2	68 ± 4
c/a ratio	0.50 ± 0.01	0.50 ± 0.02	0.52 ± 0.01	0.53 ± 0.01	0.54 ± 0.01	0.49 ± 0.02
b/a ratio	0.79 ± 0.01	0.81 ± 0.02	0.80 ± 0.01	0.80 ± 0.02	0.80 ± 0.01	0.81 ± 0.01

Table 4. Results from simulations. Mean values and standard deviations for the different quantities describing the satellite distributions: plane width, c/a ratio and b/a ratio. The first column summarizes the results from the 24 pairs in Illustris-1-Dark, the second column from the 20 pairs in Illustris-1 and the third column from the 12 pairs in the ELVIS project.

and standard deviation from the 1000 random samples. This allows us to build a normalized version of all quantities of interest by subtracting the mean and dividing between the standard deviation of the randomized samples. These normalized quantities are used to build the explicit probability distributions for the scalars describing asphericity.

3.4 Building an explicit asphericity probability distribution

After building the normalized variables with the simulated data we perform a Kolmogorov-Smirnov test with the null hypothesis of belonging to a normal distribution with mean and standard deviation computed from the mean and standard deviation estimated from the data. Although the physical quantities of interest are bound, unlike the random variables from a normal distribution, we find that the distributions for the normalized w , c/a and b/a are indeed consistent with gaussian distributions.

Based on this result we build a multivariate normal distribution for the joint distributions of the normalized w , c/a and b/a :

$$p(X; \mu, \Sigma) = \frac{1}{(2\pi)^{3/2} |\Sigma|^{1/2}} \exp \left(-\frac{1}{2} (X - \mu)^T \Sigma^{-1} (X - \mu) \right), \quad (2)$$

where $X = [w, c/a, b/a]^T$ is a vector variable with the normalized quantities, μ is the vector mean and the Σ is the covariance matrix.

We compute the preferred covariance matrix and the mean distribution values with a jackknife technique. That is, out of the n pairs in each simulation, we perform n different covariance and mean value measurements using

only $n - 1$ pairs. The reported covariance and mean values correspond to the average of all measurements, the corresponding standard deviation also helps us to estimate the uncertainty on every reported coefficient. This compact description allows us to generate samples of size N that are consistent by construction with their parent simulation.

Finally, we use the generated samples to estimate how common are the deviations from sphericity that we measure in the observational data. We use a double-tailed test in this comparison, meaning that we always measure the fraction of points with absolute values larger than the threshold absolute observed value.

4 RESULTS

Table 3 and Table 4 summarize the mean values and uncertainties for the plane w , c/a ratio and b/a ratio in the observations and simulations, respectively. The uncertainty in the observations is computed from the results with different number of satellites; in the simulations it corresponds to the standard deviation over different halos.

The observed widths w are always smaller than its randomized version. For M31 there is barely a ratio of 0.92 between observed and randomized, while for the MW this factor goes down to less than half 0.48. The observed c/a ratio follows the same extreme trend for the MW compared to a M31 distribution closer to spherical. The b/a ratio is statistically the same between observations and the spherical randomization. This confirms the extreme planar distribution for the MW and the more spherical distribution for the M31.

In the following subsections we describe in detail the results on the distributions for w , c/a and b/a . The plots

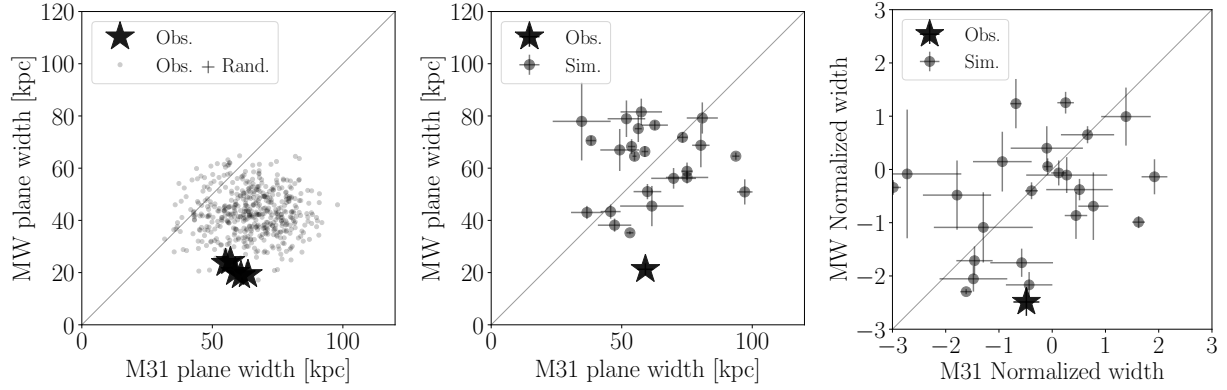


Figure 1. Plane width characterization in observations and simulations (Illustris-1-Dark in this case). In all panels the horizontal/vertical axis corresponds to the M31/MW or the most/less massive halo in the pair. Left. Plane width in physical units comparing the results from observations (stars) against the result of spherically randomizing the satellite positions (circles). Middle. Average from the observations (star) and the average from each pair in the simulation (circles). Right. Same as the middle panel except that this time each point has been normalized (median subtracted and normalized by the standard deviation) to the results of its randomization. The main message of these panels is that the MW has a significantly thinner plane both compared to the result of its own satellite spherical randomization (left panel) and the expectation from simulations (middle and right panel). This low value is 2σ away from what is expected in a spherical distribution. In M31 the satellite distribution is in agreement with the expectations both from a spherical distribution and the results from the simulations.

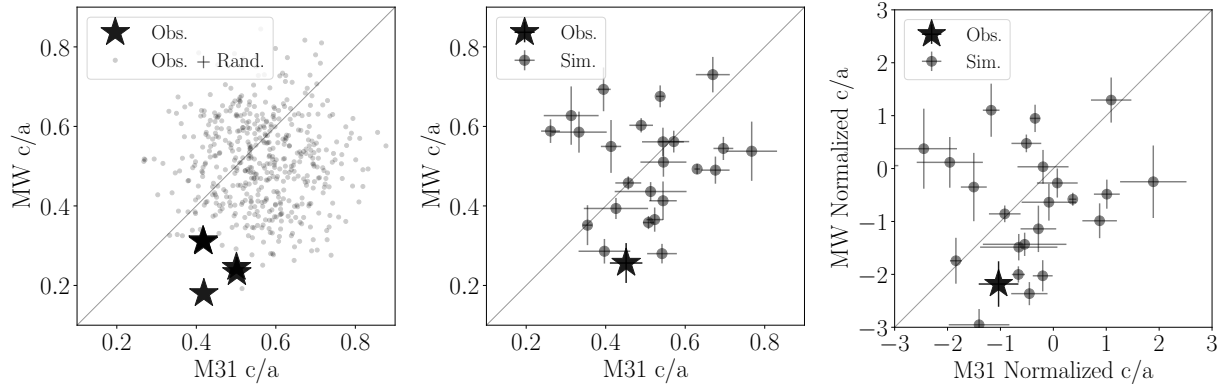


Figure 2. Same layout as in Figure 1. This time for the c/a axis ratio. The same message holds in this case; namely, that the MW has a significantly lower c/a value than the expectation from the spherical distribution and from the simulations. This low value is also 2σ away from the expectations for a spherical distribution. On the other hand, M31 is consistent both with a spherical distribution and with the results from simulations.

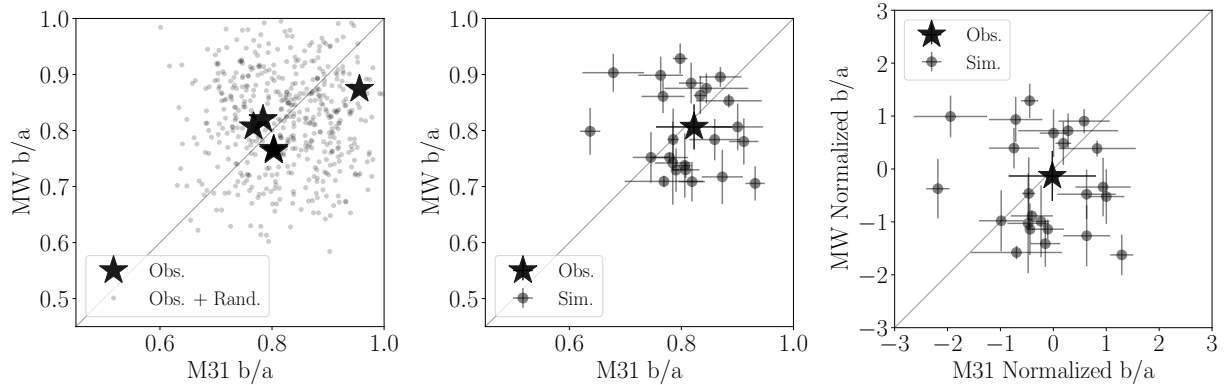


Figure 3. Same layout as in Figure 1. This time for the b/a axis ratio. In this case both the MW and M31 are consistent with the results of a spherical distribution and the simulations.

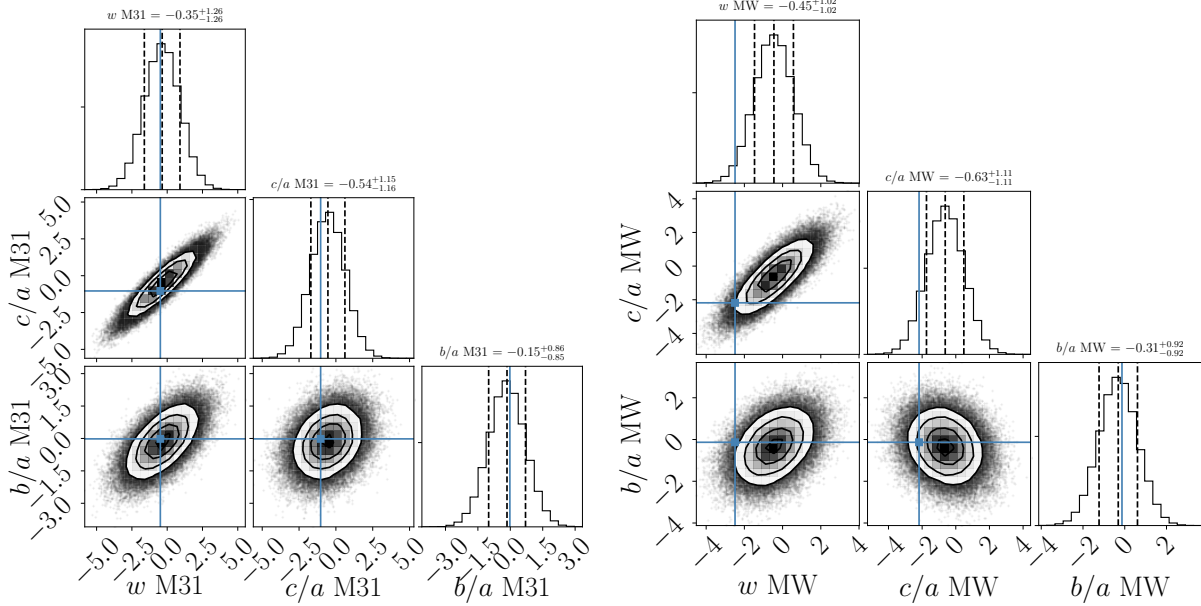


Figure 4. Results from multivariate gaussian model fitted to the normalized values for the plane width w , c/a ratio and b/a ratio from the Illustris-1-Dark results. Left/right panel correspond to M31/MW respectively. The cross indicates the observed values. The contour levels in the 2D histograms correspond to the 1σ , 2σ and 3σ contours in two dimensions. The dashed vertical lines in the histograms along the diagonal correspond to the 1σ boundaries in one dimension. The results for the gaussian model are built from 10^6 point realizations in the three-dimensional space spanned by the variables of interest for each halo. This plot clearly shows how the M31 results are well within the expectations from simulations while the MW has an unusual low value for the plane width and the c/a axis ratio.

in the main body of the paper correspond to the Illustris-1-Dark simulation; the results from the other simulations are included in the Appendix C.

4.1 Plane Width

Figure 1 summarizes the results for the width measurements. The left panel compares the results for the MW and M31 observations (stars) against its spherically randomized satellites (circles). The most interesting outcome is that the MW plane width is smaller than $\approx 98\%$ of the planes computed from the randomized distribution, while the M31 plane width is only slightly smaller than the average of the distribution.

The middle panel in Figure 1 compares the observational result (star) against the measurements of all pairs from the Illustris1-Dark simulation (circles). In this case we have a similar result as before. The observed MW width is smaller than all the results in the simulation, there is not a single halo with similar values. On the other hand, the results for the M31 are entirely consistent with observations. Most of the halos in the simulation show a width value similar to M31.

The right panel in Figure 1 shows the result for the normalized width. This panel tells the same story as the middle panel. The M31 values are typical while the MW is an outlier. The added value of the data in this panel is that it is the normalized which is consistent with normal distributions. This is the data used to build the mean values vector and covariance matrix described in Equation 2.

4.2 c/a axis ratio

Figure 2 shows the results for the minor to major axis ratio. The layout is the same as in Figure 1. The results for the c/a ratio follow the same trends as for the width w .

The left panel in Figure 2 shows how the MW c/a ratio is significantly lower than the measured values for spherical distributions, and it is smaller than $\approx 98\%$ of the randomized distributions. On the other hand the ratio for M31 is lower than the mean of the spherical values but still well within its variance. The middle panel in the same Figure shows the LG compared against the results in the simulations. In this case we find a similar trend as before. The MW is atypical and M31 is within the variance from the simulation data. This time, however, there are two MW-like halos out of the total of 24 that show an c/a as small as that of the MW. The right panel shows the normalized results. The MW shows a low c/a ratio close to between two and three standard deviations away from the mean value of the spherical distribution; this contrasts with the results for M31 which are close to 1 standard deviation away.

4.3 b/a axis ratio

Figure 3 shows the results for the minor to major axis ratio with the same layout as Figure 2. In all cases of comparison (against randomized distribution and simulations) the results for both the MW and M31 are typical.

4.4 Fit to a Multivariate Gaussian Distributions

Figure 4 illustrates the results from computing the covariance matrix and mean vector in Eq.2 from the normal-

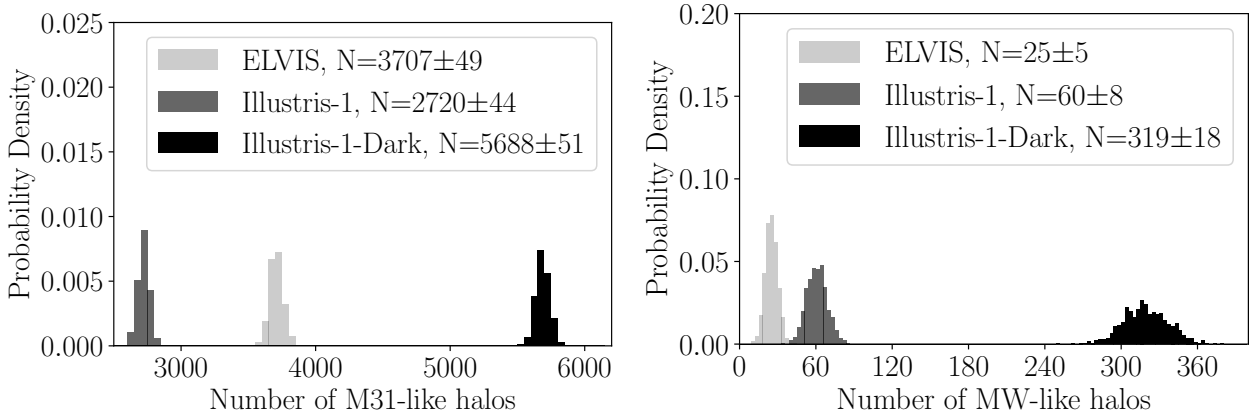


Figure 5. Probability distribution for the expected number of M31 and MW halos showing the same degree of atypicality as the Local Group if drawn from a sample of 10^4 isolated pairs. The distributions correspond to results derived from Illustris-1-Dark, Illustris-1, and ELVIS data. In the most optimistic case (Illustris-1-Dark), 1% of the pairs have two halos with properties similar to the LG. In the case of Illustris-1 this percentage drops to 0.1% and 0.01% for ELVIS.

ized quantities obtained from the Illustris-1-Dark simulation. The distributions in this Figure are computed from 10^6 points generated with the multivariate gaussian. Similar plots for Illustris-1 and ELVIS are in the Appendix C. The values for all the covariance matrices and mean vectors corresponding to all the simulations are listed in the Appendix B.

This result nicely summarizes the results we had in the previous sections. The left hand triangular plot shows how M31 falls into the middle of all 2D distributions and is always close to the peak and within the 1σ range. The right hand plot clearly places the MW observations outside the 3σ range in the joint distributions that involve the width w .

In both cases the strongest positive correlation is present for the width and the c/a axis ratio. A weaker correlation is present for the width and the b/a axis ratio.

4.5 Number of Expected LG Systems

We use the fits to the multivariate gaussian distributions to compute the expected number of pairs with characteristics similar to those of the LG. To do this we generate 10^3 samples, each sample containing 10^4 pairs, where each pair member is drawn from the corresponding multivariate gaussian distribution.

We consider that a sampled system is similar to the M31/MW galaxy if the distance of each of its normalized characteristics (w , c/a , b/a) to the sample mean is equal or larger than the distance of the observational values to the sample mean. That is, we perform a double-tailed test using the observational values as a threshold.

Figure 5 summarizes the results from this experiment. The left panel shows the probability density for the number of M31 systems in a parent sample of 10^4 pairs, the right panel shows the results for the MW. For M31, between 27% and 56% of the pairs have a satellite distribution as aspherical as the observed in M31. This fraction drops dramatically for the MW where only 0.02% to 3% of the satellites are expected to have as extreme aspherical distributions as the MW.

Considering the joint distribution of M31 and MW we

find that at most 2% of the pairs are expected to be similar to the LG. In a three dimensional gaussian distribution, having a 1σ , 2σ and 3σ interval corresponds to having respectively 19%, 73% and 97% of the total of points in the distribution. With this result in mind the LG has the same degree of atypicality as a 3σ outlier.

Among the three simulations, the results inferred from ELVIS data show the lowest fraction of M31 and MW systems; for Illustris-1-Dark we have the highest fraction of M31/MW systems. The results from Illustris-1 are in between these two, but closer to ELVIS.

The most probable reason for these trends is the different median mass for the MW/M31 halos in the pairs from these simulations. For instance for the MW halo the median maximum circular velocity is $\sim 160 \text{ km s}^{-1}$, $\sim 150 \text{ km s}^{-1}$ and $\sim 120 \text{ km s}^{-1}$ in the ELVIS, Illustris-1 and Illustris-1-Dark simulations, respectively. For the M31 halo this median velocity is $\sim 200 \text{ km s}^{-1}$ both for the ELVIS and Illustris-1 simulations, while for the Illustris-1-Dark it is $\sim 160 \text{ km s}^{-1}$.

Another element that influences this trend is the simulated physics. This is evident in the comparison between Illustris-1 and Illustris-1-Dark. These two simulations share the same characteristics except for the inclusion of baryonic physics in Illustris-1. We find that extreme MW systems are easier to find in the DM only simulation. The results listed in Appendix B show that halos are closer to spherical once baryonic effects are included. For instance the mean value for the normalized width goes closer to zero, from -0.45 ± 0.04 to -0.17 ± 0.04 , and the same is true for the c/a ratio that changes from -0.61 ± 0.04 in the DM only simulation to -0.40 ± 0.04 in Illustris-1. We postpone a detailed quantification of this effect for a future study.

5 CONCLUSIONS

In this paper we developed and demonstrated a method to quantify the asphericity of the satellite distribution around the MW and M31. In the interest of keeping the method straightforward and robust we focus on the asphericity esti-

mates for a fixed number of the brightest satellites around each galaxy.

The method uses as a reference the spherically randomized data of the system under study (Pawlowski et al. 2017). To this end, we first measure the width and axis ratios for the satellite distributions of interest. Then, we measure the same quantities for the same set of points after the spherical randomization process. Finally, we renormalize the initial results to the mean value and standard deviation computed from the randomized data.

We found that these normalized quantities are well described by a multivariate gaussian distribution in spite of the original quantities being bound. We estimated the mean and covariance of this distributions using the results of LG pairs coming from three different numerical simulations (Illustris-1, Illustris-1-Dark and ELVIS). Finally, we compared the observational results against the distributions derived from the simulations

We found that in the best case (Illustris1-Dark) the degree of asphericity in the observed LG is only expected in 3 ± 2 pairs out of a sample of 10^4 isolated pairs. This places the LG as a 3σ outlier. The weight to explain this atypical result is not distributed equally between the MW and M31. While M31 presents a fully typical asphericity in the expectations from LCDM, the MW shows aspherical deviations in plane width and the major-to-minor axis ratio highly atypical in the framework of LCDM, confirming the original hint by Kroupa et al. (2005) and more recent results by Pawlowski et al. (2015). We estimated that with the M31 between 37% and 58% of the pairs show aspherical characteristics larger than M31, while this fraction drops to less than 1% for the MW. These fractions are robust to changes in the numerical simulations, the criteria used to define the pairs and to the methods used to estimate the parameters of the multivariate normal distribution.

The focus of our approach was building an explicit probability distributions for the observables of interest, instead of trying to find simulated objects that fulfill different observational criteria. This approach is particularly useful in the case of atypical observables as its the case of interest, as it allows for an atypicality quantification without needing to build explicit samples of objects that are already scarce and difficult to find in simulations.

An extension of this framework to outliers in higher order deviations (i.e. coherent *velocity* structures) should also be possible, provided that an explicit probability distribution for the scalars of interest can be built. The approach presented here is also useful to gauge the influence of influence of different physical elements includedes the simulation. For instance, in our case the data hints towards rounder satellite distributions in simulations that include baryonic effects.

The highly aspherical satellite distribution in the MW is another piece of information that points at an atypical configuration in LCDM. We also have the number of satellites as bright as the Magellanic Clouds, only expected in 5% of galaxies (Busha et al. 2011) and the satellite velocities around the MW with a radial/tangential anisotropy only expected in 3% of systems in LCDM (Cautun & Frenk 2017). One could also add the atypical kinematics of M31 with a very low tangential velocity, which is only expected in less

than 1% of the pairs with similar environmental characteristics (Forero-Romero et al. 2013).

This atypicality should be seen as an opportunity to constrain in great detail the environment that allowed such a pattern to emerge. Although broad correlations between LG assembly, pair kinematics, halo shapes and satellite distributions are expected in LCDM (Forero-Romero et al. 2011, 2014; Forero-Romero & González 2015; Libeskind et al. 2015), we claim that detailed studies of the satellite asphericity as a function of halo mass and cosmic web environment are still missing to understand what features in the initial conditions of our LG are responsible for the extreme features observed in its satellite distribution.

ACKNOWLEDGEMENTS

We acknowledge financial support from: Universidad de Los Andes (Colombia); COLCIENCIAS (código 120471250459, contrato FP44842-287- 2016); the European Unions Horizon 2020 Research and Innovation Programme under the Marie Skłodowska-Curie grant agreement No 73437 (LACEGAL).

REFERENCES

- Busha M. T., Wechsler R. H., Behroozi P. S., Gerke B. F., Klypin A. A., Primack J. R., 2011, *ApJ*, **743**, 117
- Cautun M., Frenk C. S., 2017, *MNRAS*, **468**, L41
- Conn A. R., et al., 2013, *ApJ*, **766**, 120
- Forero-Romero J. E., González R., 2015, *ApJ*, **799**, 45
- Forero-Romero J. E., Hoffman Y., Yepes G., Gottlöber S., Piontek R., Klypin A., Steinmetz M., 2011, *MNRAS*, **417**, 1434
- Forero-Romero J. E., Hoffman Y., Bustamante S., Gottlöber S., Yepes G., 2013, *ApJ*, **767**, L5
- Forero-Romero J. E., Contreras S., Padilla N., 2014, *MNRAS*, **443**, 1090
- Garrison-Kimmel S., Boylan-Kolchin M., Bullock J. S., Lee K., 2014, *MNRAS*, **438**, 2578
- Hinshaw G., et al., 2013, *ApJS*, **208**, 19
- Ibata R. A., et al., 2013, *Nature*, **493**, 62
- Koch A., Grebel E. K., 2006, *AJ*, **131**, 1405
- Kroupa P., Theis C., Boily C. M., 2005, *A&A*, **431**, 517
- Kunkel W. E., Demers S., 1976, in Dickens R. J., Perry J. E., Smith F. G., King I. R., eds, Royal Greenwich Observatory Bulletins Vol. 182, The Galaxy and the Local Group. p. 241
- Libeskind N. I., Frenk C. S., Cole S., Helly J. C., Jenkins A., Navarro J. F., Power C., 2005, *MNRAS*, **363**, 146
- Libeskind N. I., Frenk C. S., Cole S., Jenkins A., Helly J. C., 2009, *MNRAS*, **399**, 550
- Libeskind N. I., Hoffman Y., Tully R. B., Courtois H. M., Pomarède D., Gottlöber S., Steinmetz M., 2015, *MNRAS*, **452**, 1052
- Lynden-Bell D., 1976, *MNRAS*, **174**, 695
- McConnachie A. W., 2012, *AJ*, **144**, 4
- Metz M., Kroupa P., Jerjen H., 2007, *MNRAS*, **374**, 1125
- Pawlowski M. S., McGaugh S. S., 2014, *ApJ*, **789**, L24
- Pawlowski M. S., Kroupa P., Jerjen H., 2013, *MNRAS*, **435**, 1928
- Pawlowski M. S., Kroupa P., Jerjen H., 2014, VizieR Online Data Catalog, **743**
- Pawlowski M. S., Famaey B., Merritt D., Kroupa P., 2015, *ApJ*, **815**, 19
- Pawlowski M. S., et al., 2017, *Astronomische Nachrichten*, **338**, 854
- Sawala T., et al., 2016, *MNRAS*, **457**, 1931
- Springel V., 2010, *MNRAS*, **401**, 791

Starkenburg E., et al., 2013, [MNRAS](#), **429**, 725
 Vogelsberger M., et al., 2014, [MNRAS](#), **444**, 1518
 Wang J., Frenk C. S., Cooper A. P., 2013, [MNRAS](#), **429**, 1502
 Zentner A. R., Kravtsov A. V., Gnedin O. Y., Klypin A. A., 2005, [ApJ](#), **629**, 219

APPENDIX A: PHYSICAL CHARACTERISTICS OF THE ISOLATED PAIRS SAMPLES

APPENDIX B: COVARIANCE MATRICES AND MEAN VALUE VECTORS

B1 Illustris-1

B1.1 M31

$$\Sigma = \begin{bmatrix} 0.83 \pm 0.03 & 0.78 \pm 0.04 & 0.41 \pm 0.04 \\ 0.78 \pm 0.04 & 1.16 \pm 0.05 & -0.15 \pm 0.05 \\ 0.41 \pm 0.04 & -0.15 \pm 0.05 & 0.96 \pm 0.04 \end{bmatrix}$$

$$\mu = [-0.18 \pm 0.04 \quad -0.41 \pm 0.05 \quad -0.20 \pm 0.05]$$

B1.2 MW

$$\Sigma = \begin{bmatrix} 0.78 \pm 0.06 & 0.63 \pm 0.07 & 0.40 \pm 0.03 \\ 0.63 \pm 0.07 & 0.69 \pm 0.08 & 0.06 \pm 0.02 \\ 0.40 \pm 0.03 & 0.06 \pm 0.02 & 0.61 \pm 0.04 \end{bmatrix}$$

$$\mu = [-0.17 \pm 0.04 \quad -0.40 \pm 0.04 \quad -0.23 \pm 0.04]$$

B2 Illustris-1-Dark

B2.1 M31

$$\Sigma = \begin{bmatrix} 1.50 \pm 0.08 & 1.27 \pm 0.08 & 0.64 \pm 0.04 \\ 1.27 \pm 0.08 & 1.31 \pm 0.08 & 0.28 \pm 0.04 \\ 0.64 \pm 0.04 & 0.28 \pm 0.04 & 0.70 \pm 0.04 \end{bmatrix}$$

$$\mu = [-0.37 \pm 0.05 \quad -0.55 \pm 0.05 \quad -0.13 \pm 0.03]$$

B2.2 MW

$$\Sigma = \begin{bmatrix} 1.03 \pm 0.05 & 0.94 \pm 0.05 & 0.36 \pm 0.03 \\ 0.94 \pm 0.05 & 1.24 \pm 0.07 & -0.18 \pm 0.04 \\ 0.36 \pm 0.03 & -0.18 \pm 0.04 & 0.86 \pm 0.03 \end{bmatrix}$$

$$\mu = [-0.45 \pm 0.04 \quad -0.61 \pm 0.05 \quad -0.31 \pm 0.04]$$

B3 ELVIS

B3.1 M31

$$\Sigma = \begin{bmatrix} 1.60 \pm 0.19 & 1.22 \pm 0.14 & 0.70 \pm 0.09 \\ 1.22 \pm 0.14 & 1.08 \pm 0.10 & 0.35 \pm 0.05 \\ 0.70 \pm 0.09 & 0.35 \pm 0.05 & 0.63 \pm 0.10 \end{bmatrix}$$

$$\mu = [-0.18 \pm 0.08 \quad -0.28 \pm 0.07 \quad -0.22 \pm 0.05]$$

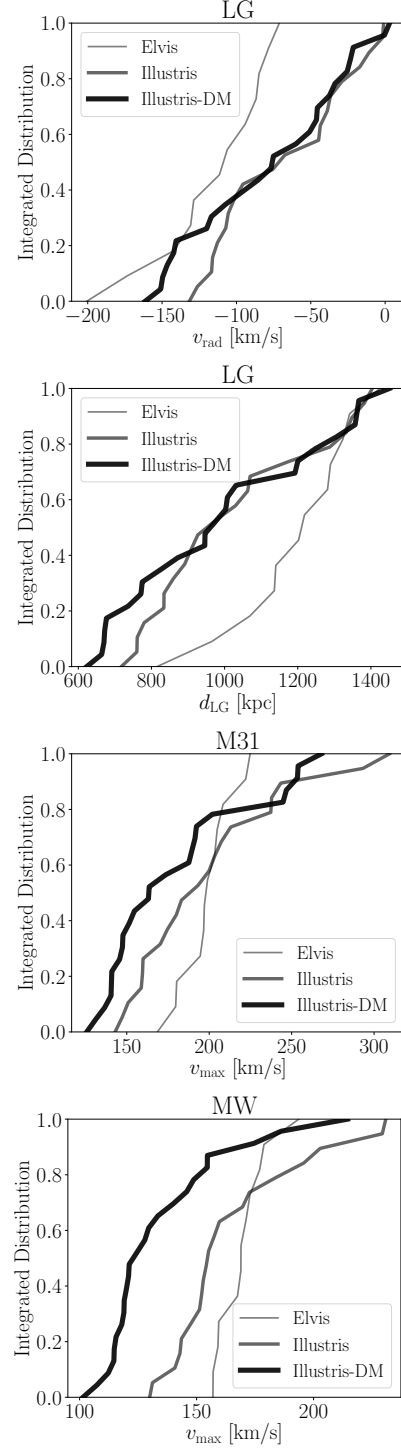


Figure A1. Physical characteristics of the LG pairs selected in the simulations. All lots show the integrated distributions. The physical properties are the radial comoving velocity between the MW and M31, the radial separation between the MW and M31 and the maximum circular velocity for the M31 and MW dark matter halo.

B3.2 MW

$$\Sigma = \begin{bmatrix} 0.45 \pm 0.04 & 0.61 \pm 0.09 & -0.11 \pm 0.09 \\ 0.61 \pm 0.09 & 1.21 \pm 0.17 & -0.63 \pm 0.09 \\ -0.11 \pm 0.05 & -0.63 \pm 0.09 & 0.64 \pm 0.06 \end{bmatrix}$$

$$\mu = [-0.32 \pm 0.04 \quad -0.74 \pm 0.07 \quad -0.08 \pm 0.05]$$

APPENDIX C: RESULTS FROM ELVIS AND ILLUSTRIS1

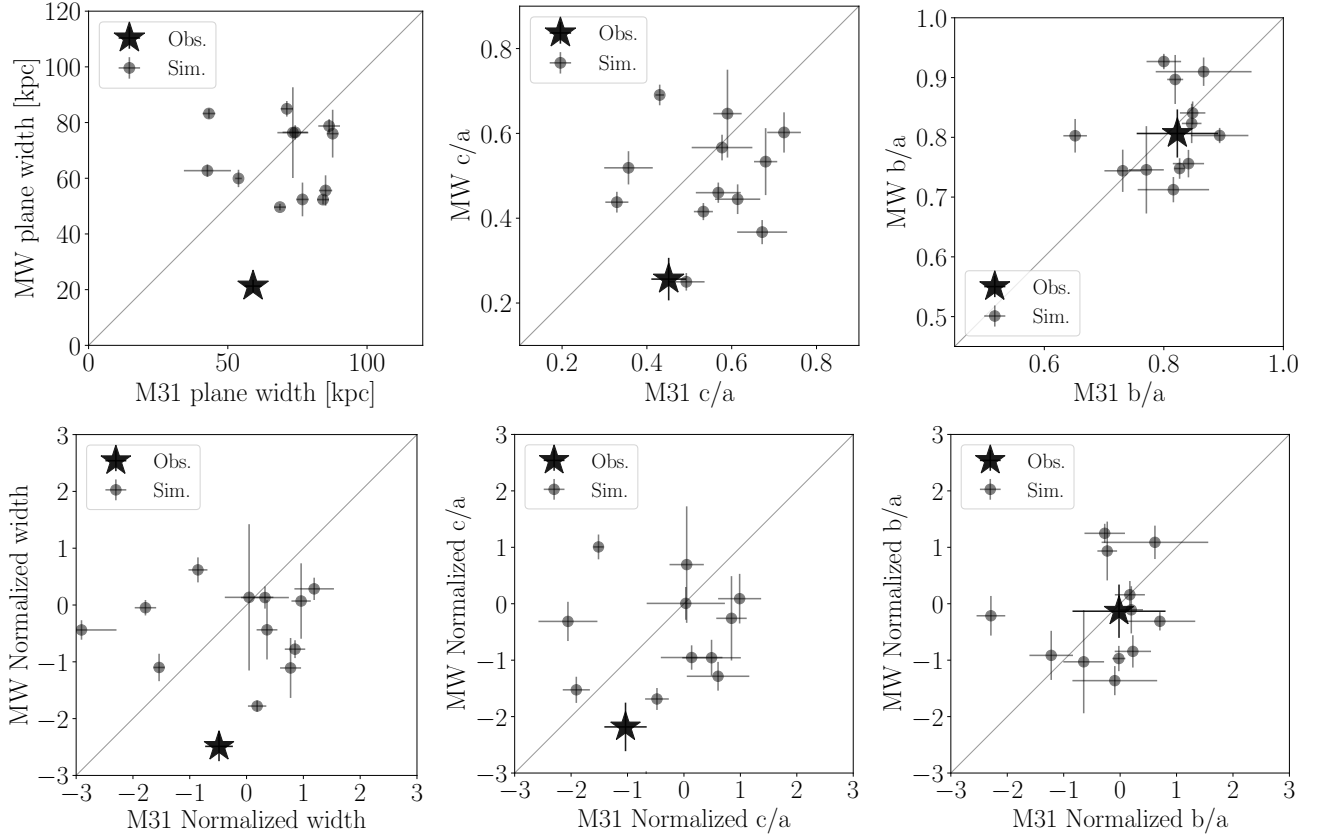


Figure C1. ELVIs results for the quantities presented for the Illustris1-Dark simulation in Figures 1, 2, 3. Upper row corresponds to the raw values from observations and simulated pairs, while the second row normalizes the same values to the mean and standard deviation on its spherically randomized counterparts.

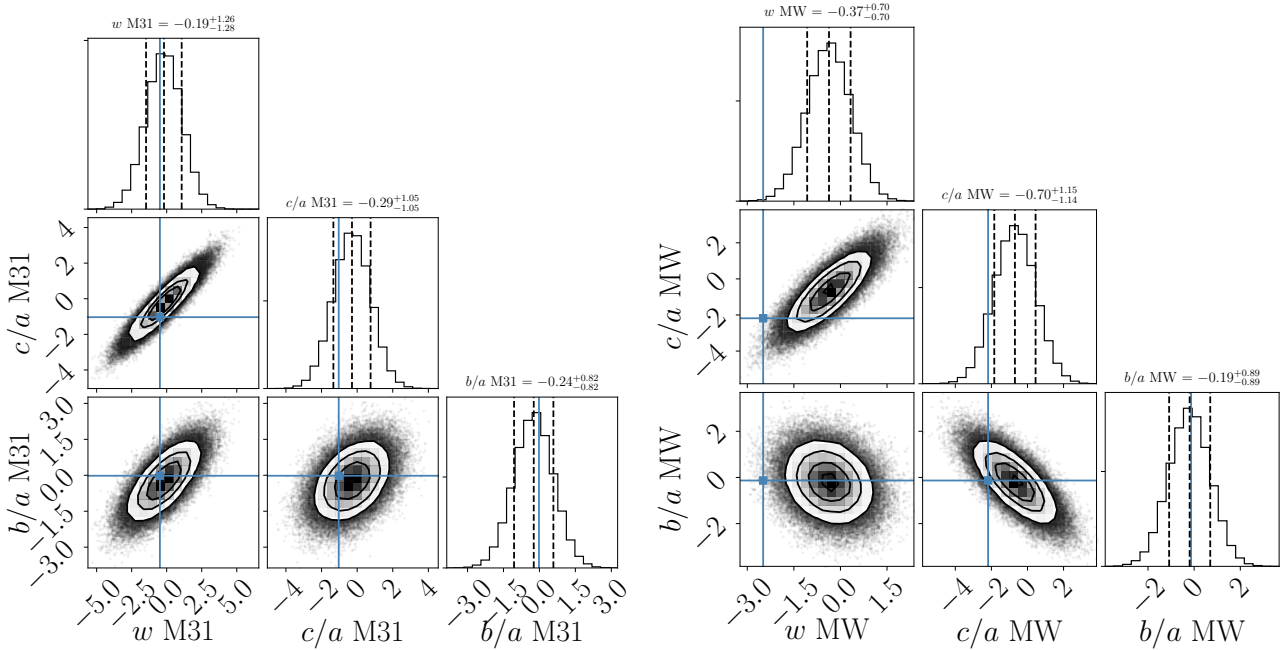


Figure C2. Same layout as Figure 4, this time computed from the ELVIS data.

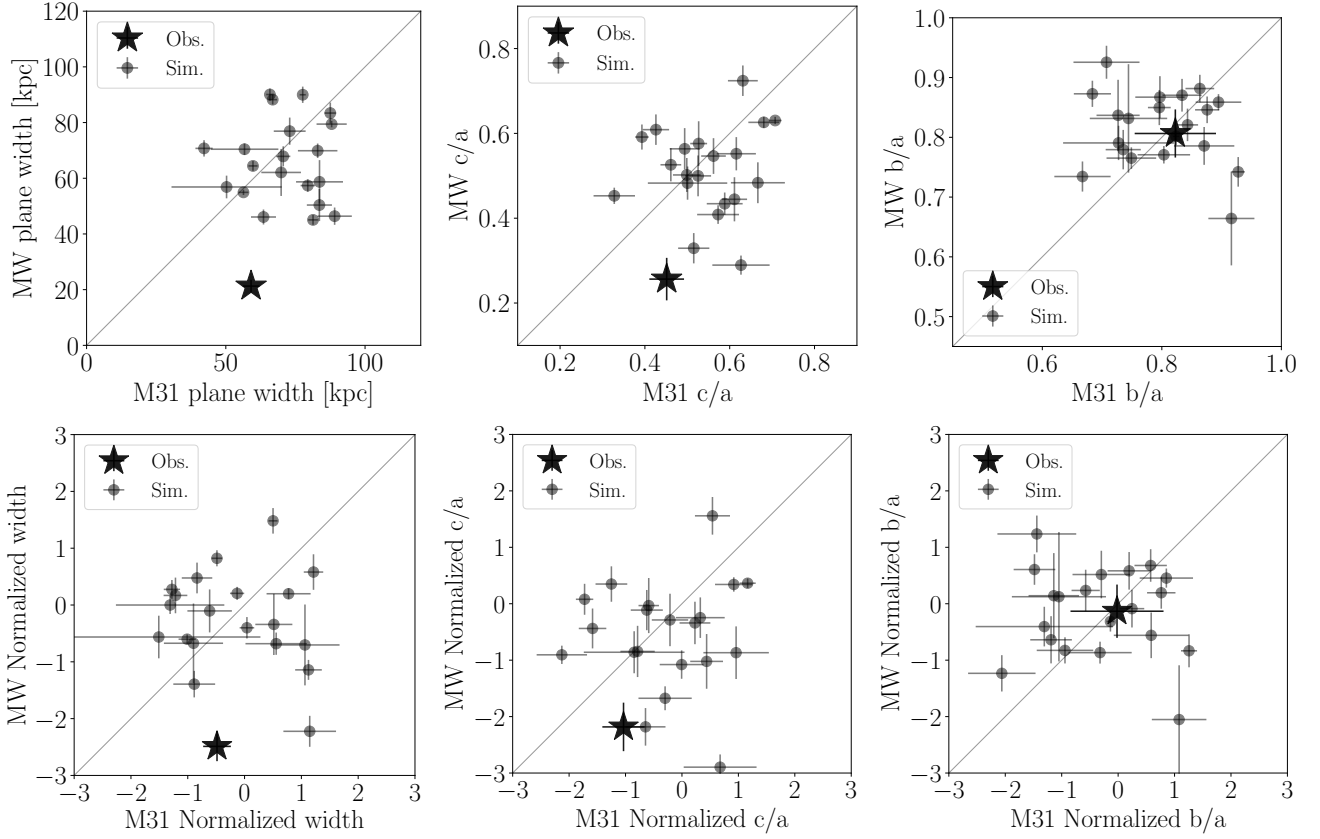


Figure C3. Same layout as Figure C1, this time computed from the Illustris-1 data.

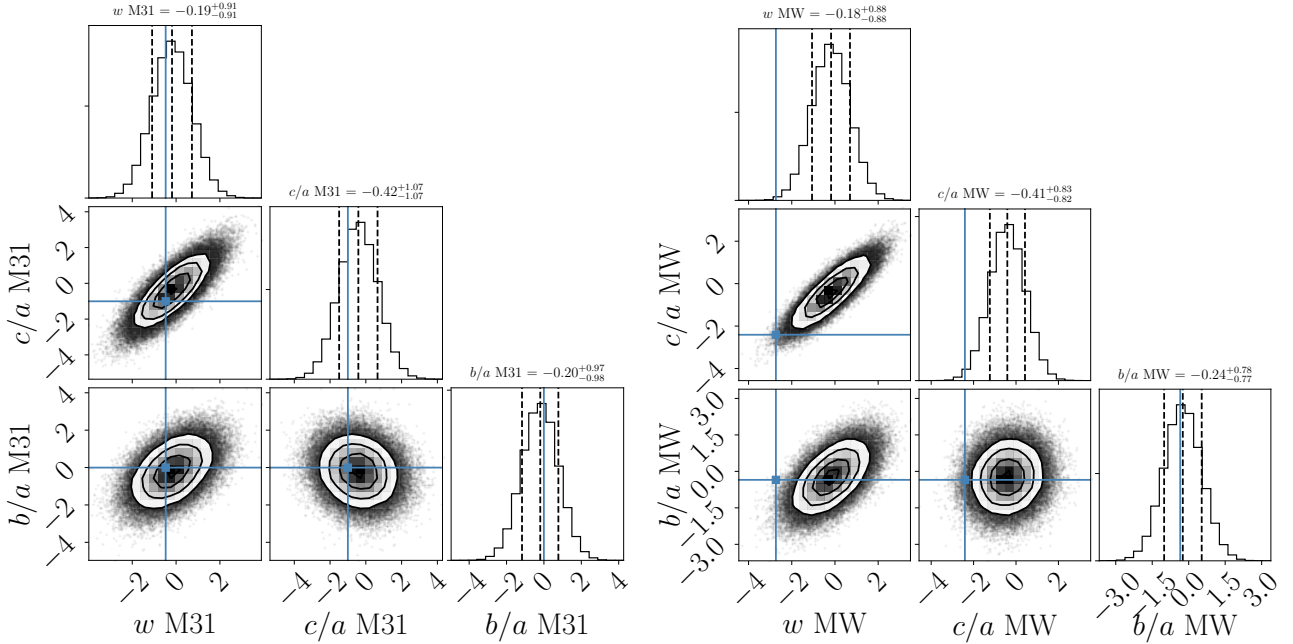


Figure C4. Same layout as Figure 4, this time computed from the Illustris-1 data.